

**Elastic scattering and  $\alpha$  production in the  ${}^9\text{Be}+{}^{89}\text{Y}$  system**C. S. Palshetkar,<sup>1,\*</sup> S. Santra,<sup>1</sup> A. Shrivastava,<sup>1</sup> A. Chatterjee,<sup>1</sup> S. K. Pandit,<sup>1</sup> K. Ramachandran,<sup>1</sup> V. V. Parkar,<sup>1</sup> V. Nanal,<sup>2</sup> V. Jha,<sup>1</sup> B. J. Roy,<sup>1</sup> and S. Kalias<sup>1</sup><sup>1</sup>*Nuclear Physics Division, Bhabha Atomic Research Centre, Mumbai 400 085, India*<sup>2</sup>*Department of Nuclear and Atomic Physics, Tata Institute of Fundamental Research, Mumbai 400 005, India*

(Received 12 March 2013; revised manuscript received 10 June 2014; published 26 June 2014)

Elastic scattering measurement for the  ${}^9\text{Be}+{}^{89}\text{Y}$  system has been carried out at near-barrier energies with the aim of investigating the effect of breakup on the elastic channel. The energy dependence of the optical model potential for the system gives an indication of the breakup threshold anomaly (BTA) for the system. An overall repulsive real part of the dynamic polarization potential (DPP) generated due to continuum couplings using the  $\alpha+{}^5\text{He}$  cluster structure for  ${}^9\text{Be}$  is consistent with the BTA behavior observed for the system. In contrast, an attractive real part of the DPP, at all energies, is observed for similar calculations carried out using the  ${}^8\text{Be} + n$  cluster structure. Coupling of the  $1n$  transfer channel in addition to continuum couplings does not have a significant effect on the elastic scattering angular distributions. The experimental  $1n$  transfer cross sections show better agreement with the corresponding values obtained using the  ${}^8\text{Be} + n$  cluster structure calculations. Inclusive breakup- $\alpha$  cross sections are observed to form a large fraction of the reaction cross sections, especially at below-barrier energies, suggesting the dominance of the breakup channel at these energies. This also supports the BTA behavior observed for the system, reflected as the presence of a reaction channel and thus the persistence of the imaginary potential at below-barrier energies.

DOI: [10.1103/PhysRevC.89.064610](https://doi.org/10.1103/PhysRevC.89.064610)

PACS number(s): 25.70.Bc

**I. INTRODUCTION**

Reaction studies with weakly bound nuclei have been a topic of interest for more than two decades [1,2]. Due to their low breakup threshold energies, it is expected that the breakup channel will have a significant effect on the reaction channels, leading to results obtained for reaction observables that differ from those obtained from reaction studies with tightly bound nuclei. Further, data from measurements with weakly bound nuclei have been used in astrophysical reaction calculations for understanding the nucleosynthesis process and studying nuclei near drip lines. The availability of radioactive ion beams has further renewed interest in studying reactions with weakly bound stable nuclei. It is suggested that due to the similar properties of weakly bound stable and unstable nuclei, reaction studies with the former can be helpful in understanding the dynamics of the reaction in the latter. In addition, the higher beam intensities of the weakly bound stable nuclei, as compared to the unstable ones, help in obtaining very good statistics during data collection and thus better interpretation of results obtained from the comparison of experimental data and calculations. Strong coupling between the reaction channels, found to occur at near-barrier energies, has made reaction studies in this energy region popular. Two types of reaction investigation have been extensively carried out: (i) Investigation of the energy dependence of the optical model potential (OMP) in elastic scattering measurements and (ii) investigation of enhancement or suppression of the complete fusion (CF) cross sections as compared to the coupled-channels (CC) calculations which exclude the continuum couplings.

In the case of tightly bound nuclei, the threshold anomaly (TA) has been observed [3] in the energy dependence of the OMP, where the real part of the potential shows a bell-shaped maximum at near-barrier energies before reducing towards zero. The corresponding imaginary part remains more or less constant at above-barrier energies and reduces towards zero at below-barrier energies. The reduction of the imaginary part, for decreasing projectile energies below the Coulomb barrier, is understood to be due to the closure of nonelastic channels and thus no absorption from the elastic channel. The real and imaginary parts have been found to be related by a dispersion relation, which explains the observed bell-shaped maximum of the real part at near-barrier energies [4]. In contrast to the observations involving tightly bound nuclei, the breakup threshold anomaly (BTA) has been observed in those involving weakly bound stable nuclei. Here, the imaginary part of the OMP increases at energies below the Coulomb barrier while the corresponding real part shows a slight reduction in the same energy region. This is suggested to be due to the influence of the breakup channel on the elastic channel. To understand this, continuum discretized coupled-channels (CDCC) calculations are carried out, in which coupling of the elastic channel with the continuum states of the nuclei is done. This is found to generate a repulsive real part of the dynamic polarization potential (DPP) which would reduce the nuclear potential and thus increase the barrier height of the effective total potential at near-barrier energies. As a result, enhanced elastic scattering cross section due to more reflection at the barrier can be expected. This is in contrast to an attractive DPP, obtained by coupling of the bound excited states of tightly bound nuclei.

The BTA has been observed in the elastic scattering of  ${}^6\text{Li}$  from heavy-mass targets while the TA has been observed for  ${}^7\text{Li}$  scattering [1]. For similar measurements carried out using  ${}^9\text{Be}$  as projectile, no definite conclusion has been reported for

\* asckj1@yahoo.co.in

the energy dependence in the  ${}^9\text{Be}+{}^{12}\text{C}$  system [5]. Studies for the  ${}^9\text{Be}+{}^{64}\text{Zn}$  system [6] did not conclusively demonstrate TA or BTA behavior. However, in a later study [7] the system is inferred to exhibit the BTA. In the case of the  ${}^9\text{Be}+{}^{27}\text{Al}$  [8] and  ${}^9\text{Be}+{}^{144}\text{Sm}$  [9] systems, the real and imaginary parts have been split into direct and fusion reactions. The imaginary part for fusion has been found to exhibit the normal TA, similar to that found for tightly bound nuclei. The imaginary part corresponding to the direct reaction is reported to show an increasing trend accompanied by a slight reduction in the real part in the same energy region. From these studies, indications of the BTA for both systems have been reported. Studies for the  ${}^9\text{Be}+{}^{208}\text{Pb}$  [10] system suggest the presence of the TA. However, from the results of a recent measurement [11] for the system, the imaginary part of the OMP has been found to be increasing with decreasing beam energy below the barrier, suggesting a departure from the earlier result of the TA for the system. A similar result has been observed for the  ${}^9\text{Be}+{}^{209}\text{Bi}$  system [12]. With the aim of investigating the effect of breakup on the elastic channel and to investigate the energy dependence of the optical potential in the elastic scattering of  ${}^9\text{Be}$  from a medium-mass target in the region  $A \sim 100$ , an elastic scattering measurement of  ${}^9\text{Be}$  from  ${}^{89}\text{Y}$  has been carried out.

The paper is organized as follows: The experimental details of the  ${}^9\text{Be}+{}^{89}\text{Y}$  scattering measurement are given in Sec. II. The optical model analysis (OMA) of the elastic scattering angular distributions is described in Sec. III A. The CDCC calculations carried out for the system are detailed in Sec. III B while the  $1n$  transfer calculations done within the coupled reaction channels (CRC) framework are described in Sec. III C. Results and discussion of the inclusive breakup- $\alpha$  cross sections obtained from the data are described in Sec. IV. Results from a simultaneous description of the elastic and the fusion channels along with a comparison of the reaction cross sections for nearby systems are discussed in Sec. V. Conclusions from the results along with a summary of the experimental investigation are given in Sec. VI.

## II. EXPERIMENTAL DETAILS

The experiment was performed at the Pelletron-Linac Facility at TIFR, Mumbai, India. The experiment was set up inside a 1-m-diameter scattering chamber having two rotatable arms. Silicon surface barrier (SSB) detectors in the  $\Delta E$ - $E$  telescopic arrangement were used to detect the elastically scattered  ${}^9\text{Be}$ . Three such telescopes (thickness  $\Delta E \sim 25$ – $33 \mu\text{m}$  and  $E \sim 500$ – $1000 \mu\text{m}$ ) were mounted on one arm. Collimators of 5 mm diameter were used at the entrance of each telescope, which provided solid angle definition. The distance between the telescopes from the target center was 20 cm. The angular separation between each telescope was  $10^\circ$ . Another SSB detector (of thickness  $\sim 60 \mu\text{m}$ ) was fixed on the other arm at an angle of  $25^\circ$  with respect to the beam axis to serve as a monitor.  ${}^9\text{Be}$  beam was bombarded onto a  $650 \mu\text{g}/\text{cm}^2$  self-supporting  ${}^{89}\text{Y}$  target. The angular distribution of the outgoing charged particles was measured at  $E_{\text{lab}} = 19$ – $33.5$  MeV in steps of  $\sim 2$  MeV for angles in the range  $\theta_{\text{lab}} = 15^\circ$ – $175^\circ$  with systematic uncertainties in

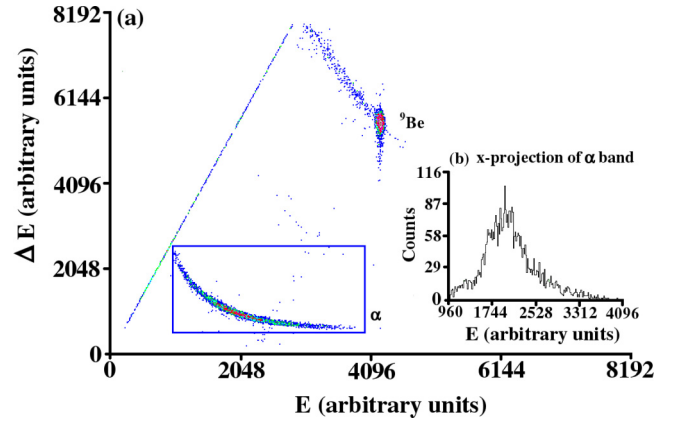


FIG. 1. (Color online) (a) Typical gain-matched  $\Delta E$ - $E$  spectrum obtained at a  ${}^9\text{Be}$  beam energy of 29 MeV and at a telescope angle of  $75^\circ$  and (b)  $x$  projection of the  $\alpha$  band [marked by the box in (a)] with the  $\alpha$  peak centered around energy  $\sim 4/9 E({}^9\text{Be})$  MeV.

angles of about  $0.05^\circ$  (i.e., the least count of the angular scale). The statistical uncertainties on the data are between  $\sim 0.6\%$  at forward angles and  $\sim 5\%$  at backward angles for all energies. Errors on the absolute normalization are  $\sim 1\%$  and those on the solid angle are  $\sim 1.3\%$ . A beam current between 5 and 15 nA was obtained during the entire duration of the experiment. Figure 1(a) shows a typical gain-matched  $\Delta E$ - $E$  spectrum obtained in the experiment.

## III. RESULTS AND DISCUSSION

### A. Optical model analysis

The experimental cross sections, plotted as a ratio of the elastic ( $\sigma_{el}$ ) to the Rutherford ( $\sigma_{\text{Ruth}}$ ) cross section as a function of the scattering angle of the  ${}^9\text{Be}$  ejectile, are shown in Fig. 2. The errors on the experimental data points (unfilled circles) are only statistical. OMA for the system was performed using the code FRESKO [13], version FRES 2.8. The angular distributions were calculated at the beam energies at the center of the target, obtained by correcting them for the energy loss in half the target thickness. The energy loss was calculated using the program SRIM [14] and was found to be  $\sim 300$  keV for above-barrier ( $V_b \sim 24$  MeV in laboratory) energies and  $\sim 400$  keV for below-barrier energies. An optical potential of the form  $U(r) = V_c(r) - V(r) - iW(r)$  was used for the calculations, where  $V_c(r)$  is the Coulomb potential, and  $V(r)$  is the real part and  $W(r)$  the imaginary part of the nuclear potential, taken to be of the Woods-Saxon form. The OMA was carried out using two different forms for the real part. In the first, OMA1,  $V(r)$  was taken equal to  $|\lambda_r V_F|$  where  $\lambda_r$  is an energy-dependent normalization factor and  $V_F$  is the microscopic double-folding potential given by [15]

$$V_F(r) = \int \int \rho_p(\vec{r}_p) \rho_t(\vec{r}_t) v(r_{pt}) d\vec{r}_p d\vec{r}_t \quad (1)$$

and  $v(r_{pt})$  is the nucleon-nucleon potential taken to be of the M3Y form:

$$v = 7999 \frac{e^{-4r}}{4r} - 2134 \frac{e^{-2.5r}}{2.5r} + J_{00} \delta(r_{pt}^2), \quad (2)$$

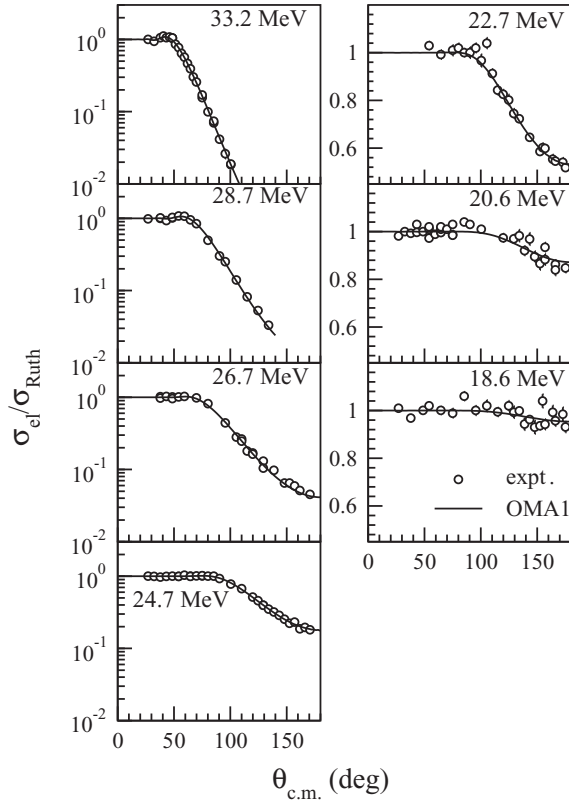


FIG. 2. Ratio of the experimental elastic scattering cross section to the Rutherford cross section as a function of center-of-mass angle of the  $^9\text{Be}$  ejectile, at different energies (the error bars are within the point size). The solid lines are the cross sections obtained from OMA1.

where  $J_{00} = -262 \text{ MeV fm}^3$  and corresponds to the single-nucleon knockout exchange. The nucleon density distribution for  $^9\text{Be}$  ( $\rho_p$ ) was obtained from Ref. [16] and the charge density for  $^{89}\text{Y}$  ( $\rho_t$ ) was obtained from Ref. [17].

The microscopic double-folding potential was obtained by using the code DFPOT [18]. This real potential along with the Coulomb potential with  $r_c = 1.26 \text{ fm}$  and a Woods-Saxon form for the imaginary potential were given as input to FRESKO with initial parameters  $\lambda_r = 1.0$ ,  $W_o = 20.0 \text{ MeV}$ ,  $r_w = 1.22 \text{ fm}$ , and  $a_w = 0.65 \text{ fm}$ . The radius parameter  $r_i$  with  $i = c, o, w$  is taken here in the heavy-ion convention with  $r = r_i(A_p^{1/3} + A_t^{1/3})$ . The search option SFRESKO was then

employed to get the best fit to the experimental data, keeping  $r_w$  fixed at the value of  $1.22 \text{ fm}$ . Table I gives the best-fit parameters for each energy (corrected for energy loss in half the target thickness) along with the reaction cross sections and their uncertainties due to errors on the potential parameters. We mention here that at the lowest energy ( $18.6 \text{ MeV}$ ) it was not possible to obtain an error on  $\lambda_r$  as it could be arbitrarily varied to any value and a fit to the experimental angular distribution could still be obtained with a similar  $\chi^2/N$ . Thus its error is taken the same as the value of  $\lambda_r$ . The solid lines in Fig. 2 represent the  $\sigma_{el}/\sigma_{Ruth}$  values obtained using these best-fit potential parameters.

In the second method, OMA2, both the real and imaginary parts of the OMP were taken to have a Woods-Saxon form. The initial parameters of  $V_o = W_o = 20.0 \text{ MeV}$ ,  $r_{o,w} = 1.22 \text{ fm}$ , and  $a_{o,w} = 0.65 \text{ fm}$  were taken as input potential parameters for the calculations. SFRESKO was employed to find the best-fit parameters, keeping all six parameters of the total nuclear potential variable. The resultant values along with the reaction cross sections and their uncertainties due to errors on individual parameters thus obtained are given in Table II. The  $\sigma_{el}/\sigma_{Ruth}$  values obtained using these best-fit parameters overlap the corresponding values obtained from OMA1 and are thus not plotted in Fig. 2. As in OMA1, the error on  $V_o$  at  $18.6 \text{ MeV}$  is taken to be the same as the value of  $V_o$  because of the difficulty in obtaining the error as mentioned above.

In order to investigate the energy dependence of the optical potential, the real and imaginary parts of the OMP are required to be plotted at the radius of sensitivity. This radius was obtained by two different methods. In the case of OMA1, the strong absorption radius was calculated at different beam energies using the formula for the distance of closest approach for the Coulomb trajectories:

$$R_{sa} = \frac{\eta}{k} \left[ 1 + \left\{ 1 + \left( \frac{L_{1/2}}{\eta} \right)^2 \right\}^{1/2} \right] \quad (3)$$

where  $\eta$  is the Sommerfeld parameter,  $k$  is the wave number, and  $L_{1/2}$  is the partial wave angular momentum for which the transmission coefficient becomes 0.5 (see Table I for the values). An average value of  $R_{sa}^{av} = 10.58 \text{ fm}$  was obtained. In the case of OMA2, the radius parameters  $r_o$  and  $r_w$ , obtained from the best-fit values at each energy (Table II), were kept constant and  $a_o$  and  $a_w$  were varied in steps of  $0.1 \text{ fm}$ . The strengths of the real and imaginary parts were kept variable. SFRESKO was employed to get the best fit to the experimental

TABLE I. Best-fit optical potential parameters from OMA1 with  $r_w = 1.22 \text{ fm}$  fixed.

$E_{lab}$ (MeV)	$\lambda_r$	$W_o$ (MeV)	$a_o$ (fm)	$\chi^2/N$	$\sigma_R$ (mb)	$R_{sa}$ (fm)	$V(10.6)$ (MeV)	$W(10.6)$ (MeV)
33.2	$1.74 \pm 0.08$	$25.02 \pm 1.78$	$0.70 \pm 0.01$	6.81	$1176 \pm 37$	10.63	$0.40 \pm 0.02$	$0.51 \pm 0.04$
28.7	$1.61 \pm 0.06$	$25.01 \pm 1.93$	$0.64 \pm 0.01$	3.04	$733 \pm 24$	10.46	$0.37 \pm 0.02$	$0.37 \pm 0.03$
26.7	$1.50 \pm 0.09$	$30.75 \pm 4.18$	$0.69 \pm 0.01$	4.25	$628 \pm 49$	10.69	$0.34 \pm 0.02$	$0.58 \pm 0.09$
24.7	$1.54 \pm 0.04$	$15.16 \pm 1.16$	$0.68 \pm 0.01$	2.59	$293 \pm 21$	10.55	$0.35 \pm 0.01$	$0.28 \pm 0.02$
22.7	$1.45 \pm 0.13$	$25.00 \pm 1.91$	$0.66 \pm 0.01$	1.83	$136 \pm 18$		$0.33 \pm 0.03$	$0.40 \pm 0.03$
20.6	$1.37 \pm 1.18$	$22.99 \pm 7.41$	$0.66 \pm 0.04$	2.59	$33 \pm 24$		$0.31 \pm 0.26$	$0.37 \pm 0.12$
18.6	$1.41 \pm 1.41$	$35.29 \pm 17.96$	$0.70 \pm 0.05$	1.96	$15 \pm 18$		$0.32 \pm 0.32$	$0.73 \pm 0.37$

TABLE II. Best-fit optical potential parameters from OMA2.

$E_{\text{lab}}$ (MeV)	$V_r$ (MeV)	$r_o$ (fm)	$a_o$ (fm)	$W_o$ (MeV)	$r_w$ (fm)	$a_w$ (fm)	$\chi^2/N$	$\sigma_R$ (mb)	$R_s^r$ (fm)	$R_s^i$ (fm)	$V(10.7)$ (MeV)	$W(10.7)$ (MeV)
33.2	$30.79 \pm 8.22$	1.22	$0.64 \pm 0.05$	$30.54 \pm 1.99$	1.22	$0.65 \pm 0.01$	5.54	$1156 \pm 81$	11.30	9.90	$0.44 \pm 0.12$	$0.47 \pm 0.03$
28.7	$24.77 \pm 1.52$	1.23	$0.66 \pm 0.01$	$34.46 \pm 0.60$	1.24	$0.56 \pm 0.01$	1.60	$716 \pm 27$	11.30	10.10	$0.45 \pm 0.03$	$0.33 \pm 0.01$
26.7	$16.14 \pm 0.03$	1.23	$0.80 \pm 0.01$	$37.02 \pm 0.01$	1.25	$0.58 \pm 0.01$	3.13	$583 \pm 35$	12.06	10.01	$0.55 \pm 0.01$	$0.49 \pm 0.02$
24.7	$24.23 \pm 0.81$	1.22	$0.64 \pm 0.01$	$19.04 \pm 1.90$	1.22	$0.65 \pm 0.01$	2.90	$293 \pm 27$	10.82	10.49	$0.35 \pm 0.01$	$0.29 \pm 0.03$
22.7	$21.38 \pm 1.39$	1.21	$0.70 \pm 0.01$	$22.26 \pm 1.73$	1.23	$0.63 \pm 0.01$	1.53	$124 \pm 18$	10.63	11.20	$0.41 \pm 0.03$	$0.35 \pm 0.03$
20.6	$24.79 \pm 10.71$	1.22	$0.70 \pm 0.08$	$21.54 \pm 7.95$	1.22	$0.64 \pm 0.04$	2.43	$28 \pm 28$	10.52	11.94	$0.50 \pm 0.22$	$0.31 \pm 0.12$
18.6	$25.56 \pm 25.56$	1.23	$0.68 \pm 0.41$	$28.31 \pm 13.60$	1.23	$0.73 \pm 0.06$	1.96	$17 \pm 42$	8.80	13.60	$0.50 \pm 0.58$	$0.70 \pm 0.34$

angular distributions. The resulting  $\chi^2/N$  of the new set was within 15% of that of the best-fit parameters. In this way, different sets of potential parameters were obtained which closely reproduced the experimental data and the radii of sensitivity  $R_s^r$  and  $R_s^i$  were found at each energy (see Table II). The average value of the sensitivity radii obtained at all energies was found to be  $R_s^{av} = 10.90$  fm. For investigating the energy dependence of the potential parameters, the average of the  $R_{sa}^{av}$  and  $R_s^{av}$  values obtained from OMA1 and OMA2 was taken to be  $R_s = 10.7$  fm. Figures 3 and 4 show the potential values obtained from OMA1 and OMA2, respectively (for values see Tables I and II) (filled circles), plotted at this radius as a function of energy.

A dispersion relation of the form [4]

$$V(r, E) = V_o(r, E) + \Delta V(r, E) \quad (4)$$

was applied between the real and imaginary parts of the OMP, where  $\Delta V$  is a rapidly varying function of energy and is called the polarization potential, and  $V_o$  is a smoothly varying function of energy. A linear segment model was used for  $W(r, E)$  and the real part was calculated from the imaginary

part using the subtracted dispersion relation [3]

$$\Delta V(E) = \Delta V(E_s) + (E - E_s) \frac{P}{\pi} \times \int \frac{W(E')}{(E' - E_s)(E' - E)} dE', \quad (5)$$

where  $P$  is the principal value of the integral,  $E_s$  is the reference energy generally chosen to be at the high-energy region under study and  $\Delta V(E_s)$  is the potential at  $E_s$ . In the current calculations, we assumed  $E_s = 35.1$  MeV and  $\Delta V(E_s) = -0.29$  MeV for OMA1 and  $\Delta V(E_s) = -0.39$  MeV for OMA2. The three linear segments used for  $W(E)$ , plotted as the solid line in Figs. 3(b) and 4(b), were used for calculating the real part using the dispersion relation. The real part is plotted as the solid line in Figs. 3(a) and 4(a). The same procedure was carried out with two more sets for the imaginary potential, having different slopes, for the purpose of comparison. One of the sets [dotted line in Figs. 3(b) and 4(b)] was chosen to have an energy dependence similar to that observed in the conventional TA. It can be seen that the dispersion relation is valid for the  ${}^9\text{Be}+{}^{89}\text{Y}$  system. Even though the dotted line can be argued to fall within the errors and the scatter of the  $W(R_s)$  values (as a function of energy), obtained from OMA1 and OMA2, the real parts are

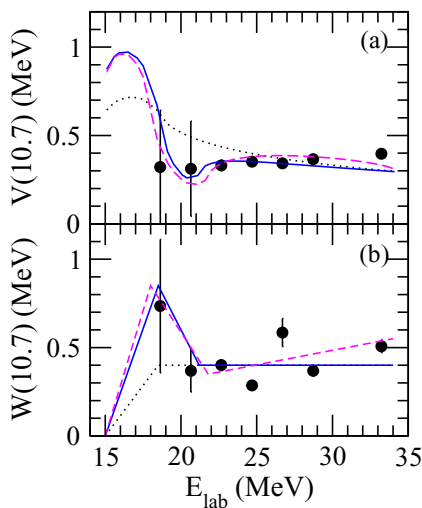


FIG. 3. (Color online) (a) Real and (b) imaginary part of the optical potential (filled circles), obtained from OMA1, as a function of the laboratory energy of the  ${}^9\text{Be}$  projectile, plotted at a radius of 10.7 fm. The lines are values obtained by applying the dispersion relation [Eq. (5)]. See text for description.

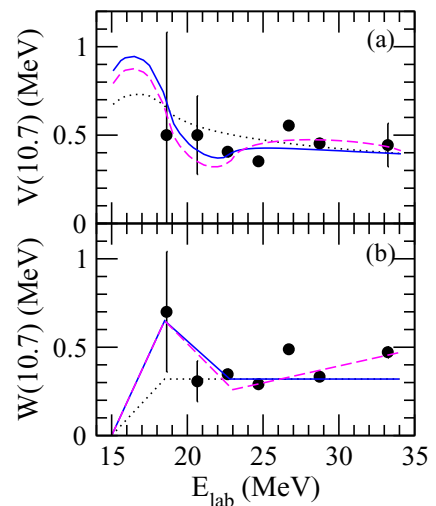


FIG. 4. (Color online) Same as Fig. 3 but with the real and imaginary parts of the optical potential obtained from OMA2.

not reproduced. In addition, the real part does not show an increasing trend with decreasing beam energy, as would be expected from a system exhibiting TA. The three-segment set represented by solid lines gives the best fit to the energy dependence of the real and imaginary parts of the OMP, even though the potential values have large error bars at energies below  $\sim 25$  MeV. In addition, the imaginary part from both OMA1 and OMA2 is seen to persist at energies even below the Coulomb barrier for the system. This indicates BTA behavior for the  ${}^9\text{Be}+{}^{89}\text{Y}$  system.

## B. Continuum discretized coupled-channels calculations

In order to investigate the effect of the breakup of  ${}^9\text{Be}$  on its elastic scattering, continuum discretized coupled-channels calculations were carried out for the system, using the code FRESKO, considering the (1)  $\alpha+{}^5\text{He}$  and (2)  ${}^8\text{Be}+n$  cluster structures for  ${}^9\text{Be}$  [19,20], with breakup threshold energies of 2.467 MeV and 1.664 MeV, respectively. For these calculations, the Woods-Saxon form have been considered for the core+valence, core+target, and valence+target nuclear potentials.

### 1. $\alpha+{}^5\text{He}$ cluster

In using this cluster structure for  ${}^9\text{Be}$ ,  ${}^5\text{He}$  was taken to be the core with  $\alpha$  as the valence. The binding potential for the  $\alpha+{}^5\text{He}$  cluster was taken from Ref. [21] with  $r_o = 1.115$  fm, and  $a_o = 0.57$  fm. As the ground state of  ${}^9\text{Be}$  has a large deformation ( $\beta \sim 1.3$ ) [22], the reorientation coupling was included in the calculations with  $L = 0$  and 2 components following the procedure given in Ref. [21]. Continuum states with  $L = 0, 1, 2$  and energies above 2.467 MeV up to 4.4 MeV were discretized in momentum space in the range  $0.15 \leq k \leq 0.45$  fm $^{-1}$  in steps of  $\Delta k = 0.15$  fm $^{-1}$ . The initial values for the  $\alpha+{}^{89}\text{Y}$  potential were obtained as follows: Fits to the experimental elastic scattering angular distribution at 16 MeV [which is close to  $4/9 \times E({}^9\text{Be})$  with  $E({}^9\text{Be}) = 33.2$  MeV, the highest energy measured in this experiment] of Ref. [23] were obtained taking initial potential parameters from Ref. [24]. The best-fit parameters  $V_o = 75.65$  MeV,  $r_o = 1.13$  fm,  $a_o = 0.52$  fm,  $W_o = 14.71$  MeV,  $r_w = 1.14$  fm, and  $a_w = 0.36$  fm were then obtained using SFRESKO. For the final calculations, the depth of the volume real part was changed to  $V_o = 87.65$  MeV and, in addition, the diffuseness parameter for the volume real part was changed to  $a_o = 0.42$  fm to obtain the best fit to the experimental elastic scattering angular distribution at the highest energy, and these values were used for calculations at all other energies. The  ${}^5\text{He}+{}^{89}\text{Y}$  potential was taken to have the same depth and radius parameter as those for  $\alpha+{}^{89}\text{Y}$  but with diffuseness parameter increased by 0.1 fm to take into account the extended structure of  ${}^5\text{He}$  as was done in Ref. [21].

In addition to the continuum, couplings to the  ${}^9\text{Be}$  excited state of  $5/2^-$  at  $E = 2.42$  MeV, taken as a bound state in this cluster structure, and the resonant state of  $7/2^-$  at  $E = 6.38$  MeV with a width of 1.21 MeV [25,26] were also included by considering them as pure  $L = 2$  states. The coupling scheme was suitably modified when including the  $7/2^-$  resonance to avoid double counting. The same potential parameters as those used for the ground state were used

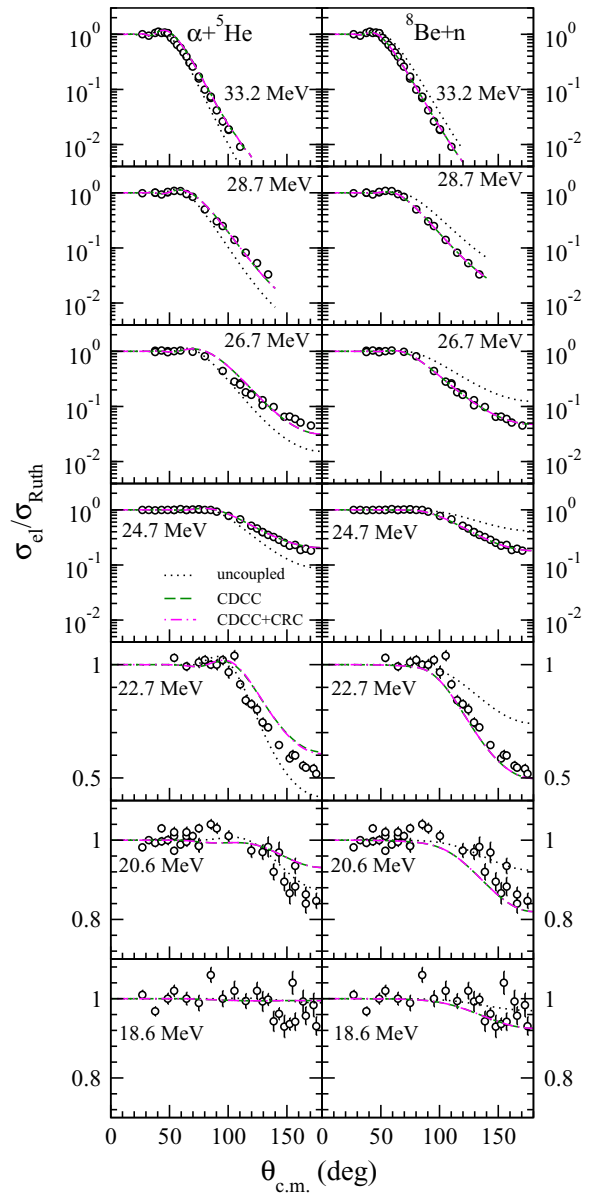


FIG. 5. (Color online) Ratio of the experimental elastic scattering cross section to the Rutherford cross section as a function of center-of-mass angle of the ejectile (the same unfilled circles as in Fig. 1) for different energies. The errors are within the point size. The dotted lines are the results without any coupling while the dashed lines are the CDCC results and the dot-dashed lines are the CDCC+CRC results obtained using the  $\alpha+{}^5\text{He}$  cluster structure for  ${}^9\text{Be}$  (left panel) and the  ${}^8\text{Be}+n$  cluster structure (right panel), respectively.

for the continuum states. To input the depth of the volume real potential for the  $7/2^-$  resonance state, the width of the resonance was binned into energy intervals of 0.05 MeV and the depth of the potential adjusted such that the cross section thus obtained peaked at the resonant state energy.

Results of the calculations including the continuum + the ground state reorientation +  $5/2^-$  excited state +  $7/2^-$  resonance state coupling (CDCC) are plotted in the left panel of Fig. 5 as dashed lines at different energies. For comparison,

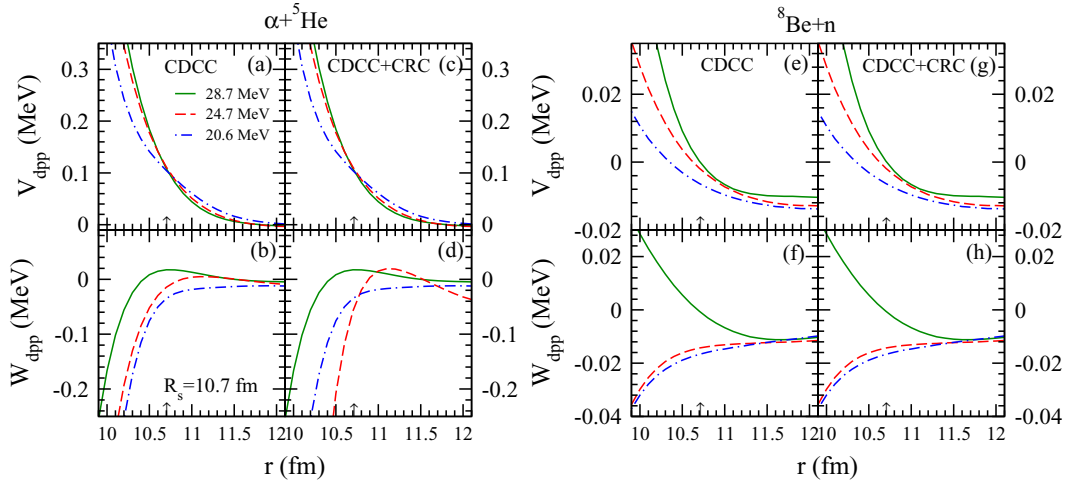


FIG. 6. (Color online) Real (a),(c),(e),(g) and imaginary (b),(d),(f),(h) parts of the DPP obtained from the CDCC and the CDCC + CRC calculations as a function of radius obtained using the  $\alpha + {}^5\text{He}$  and the  ${}^8\text{Be} + n$  cluster structures for  ${}^9\text{Be}$ .

the results obtained by excluding any couplings (uncoupled) have been plotted as dotted lines. It is observed that the CDCC results, which are in agreement with the experimental values, are enhanced as compared to the uncoupled results at backward angles, suggesting a repulsive DPP generated due to continuum coupling. To check this, the real ( $V_{\text{dpp}}$ ) and imaginary ( $W_{\text{dpp}}$ ) parts of the DPP, obtained from the calculations, have been plotted as functions of radius in Figs. 6(a) and (b), respectively. It can be seen that  $V_{\text{dpp}}$  is repulsive in nature and has very similar magnitude, for all energies, around 10.7 fm while  $W_{\text{dpp}}$  is observed to be increasingly attractive with decreasing energy, consistent with the observations in Ref. [20]. The magnitude of  $V_{\text{dpp}}$  is greater than  $W_{\text{dpp}}$  for all energies, which must be leading to an overall repulsive effect of the DPP. This would lead to an increase in the barrier height of the effective total potential and thus an enhanced elastic cross section due to more reflection at the barrier. This is consistent with the above-mentioned observation of  $\sigma_{el}/\sigma_{\text{Ruth}}$  values at all energies at backward angles. The very similar values of  $V_{\text{dpp}}$  at 10.7 fm might explain the flat distribution of  $V(10.7)$  in Figs. 3(a) and 4(a). The increasing magnitude of  $W_{\text{dpp}}$  with decreasing energy implies that the imaginary part of the nuclear potential shows an increasing trend. This is consistent with the observed trend of  $W(10.7)$  in Figs. 3(b) and 4(b).

## 2. ${}^8\text{Be} + n$ cluster

In using this cluster structure,  ${}^8\text{Be}$  was taken as the core and the neutron as the valence. The potential for binding the neutron within the  ${}^8\text{Be}$  nucleus was taken from Ref. [27] with  $r_o = 1.15$  fm and  $a_o = 0.57$  fm. Continuum states with  $L = 0, 1, 2$  and energies above the breakup threshold of 1.664 MeV up to 7 MeV were coupled by discretizing them in momentum space in the range  $0.12 \leq k \leq 0.48$  in steps of  $\Delta k = 0.12 \text{ fm}^{-1}$ . In addition to the continuum states, coupling to the  $1/2^+$  (at  $E = 1.68$  MeV) and  $5/2^+$  (at  $E = 3.04$  MeV) resonant states with widths of 0.217 MeV and 0.282 MeV, respectively [26], were included in the calculations by suitably modifying the coupling scheme. The

same procedure as mentioned in Sec. III B 1 above was used for fixing the depth of the potential for these states. Target inelastic states up to 1.75 MeV input in the calculations for generating the transfer states as described in Sec. III C below were also included in these calculations. The parameters for the  ${}^8\text{Be} + {}^89\text{Y}$  nuclear potential were taken to be the same as the  ${}^9\text{Be} + {}^89\text{Y}$  parameters obtained from OMA2 for each energy (see Table II). The  $n + {}^89\text{Y}$  potential was taken from Ref. [28] with initial parameters  $V_o = 54.14$  MeV,  $r_{o,w} = 1.22$  fm,  $a_{o,w} = 0.67$  fm,  $W_o = 0.35$  MeV,  $W_D = 4.59$  MeV,  $r_D = 1.27$  fm,  $a_D = 0.53$  fm and  $V_{so} = 5.89$  MeV,  $r_{so} = 1.05$  fm, and  $a_{so} = 0.56$  fm. The volume real part depth was adjusted to  $V_o = 5.4$  MeV to get a best fit to the experimental angular distribution at the highest energy and was used for calculations at all other energies.

Results of the calculations including the continuum + resonant states + target inelastic states (CDCC) are plotted in the right panel of Fig. 5 by the dashed lines and for comparison results excluding any couplings are plotted as the dotted lines (uncoupled). In contrast to the results obtained using the  $\alpha + {}^5\text{He}$  cluster, the uncoupled cross sections are higher than the corresponding CDCC results at backward angles, similar to the results found in [20], thus indicating an attractive overall DPP. It is also observed that there is better agreement between the experimental cross sections with the CDCC results when using the  ${}^8\text{Be} + n$  cluster structure for  ${}^9\text{Be}$ , especially at below-barrier energies, whereas results obtained from  $\alpha + {}^5\text{He}$  show a large deviation. The magnitudes of  $V_{\text{dpp}}$  and  $W_{\text{dpp}}$ , plotted in Figs. 6(e) and 6(f), are much smaller as compared to the corresponding values obtained from  $\alpha + {}^5\text{He}$  [Figs. 6(a) and 6(b)]. At above-barrier energies around 10.7 fm,  $V_{\text{dpp}}$  has a very small positive value and is thus repulsive in nature, similar to the corresponding values found for  $\alpha + {}^5\text{He}$ . But  $W_{\text{dpp}}$  has a negative value slightly larger in magnitude than  $V_{\text{dpp}}$ . Thus, in this energy region, the overall contribution to the effective potential from the DPP will cancel out and thus a smooth energy dependence can be expected. At below-barrier energies, both  $V_{\text{dpp}}$  and  $W_{\text{dpp}}$  have increasingly negative values. Thus, the nuclear potential may be expected to become more attractive

in nature with decreasing energy, reducing the barrier height of the effective total potential. As a result, reaction channels may be expected to be persistent at below-barrier energies. This agrees with the increasing values of  $W_{\text{dpp}}$  and the trend of  $W(10.7)$  observed, with decreasing energy of  ${}^9\text{Be}$ , in Figs. 3(b) and 4(b). However, the real part of the nuclear potential would be expected to increase with decreasing energy, which is in contrast to the observation of  $V(10.7)$  in Figs. 3(a) and 4(a).

### C. $1n$ transfer coupling

The  $Q$  value for the  ${}^{89}\text{Y}({}^9\text{Be}, {}^8\text{Be}){}^{90}\text{Y}$  one-neutron ( $1n$ ) transfer is +5.19 MeV. Thus, it is possible that this channel may have some effect on the elastic channel. To investigate this, the  $1n$  transfer channel was coupled, along with the inclusion of continuum coupling, to the elastic channel in the coupled reaction channels framework using the code FRESKO. Table III gives the excitation energy, spin, parity, particle configuration, and spectroscopic factor ( $C^2S$ ) [29] for the  ${}^{90}\text{Y}$  states included in the calculations. The  ${}^9\text{Be}/{}^8\text{Be}$  overlap spectroscopic factor was taken to be 0.42 [27]. For generating the form factors for the transfer states in the FRESKO calculations, the  ${}^{90}\text{Y}$  nucleus was considered as a  ${}^{89}\text{Y}$  core + 1 valence neutron. The neutron magic  ${}^{89}\text{Y}$  nucleus ( $N = 50$ ) has neutron shells completely filled up to  $1g_{9/2}$  while the odd proton is in the  $2p_{1/2}$  state. Thus, the incoming neutron will be transferred to the  $2d_{5/2}$  state and its interaction with the odd proton of  ${}^{89}\text{Y}$  in either the ground state or the excited state generates the excited states of  ${}^{90}\text{Y}$  [30]. The  $2^-$  ground state and  $3^-$  state of  ${}^{90}\text{Y}$ , at an excitation energy of 0.202 MeV, have been obtained by the coupling of the spin parity of the transferred neutron in the  $2d_{5/2}$  state with the odd proton of  ${}^{89}\text{Y}$  in the  $2p_{1/2}$  state. The positive-parity states  $7^+$ ,  $2^+$ ,  $3^+$ ,  $4^+$ ,  $5^+$ , and  $6^+$  of  ${}^{90}\text{Y}$  are constructed by first exciting the odd proton of  ${}^{89}\text{Y}$  from  $2p_{1/2}$  to the  $1g_{9/2}$  state and then coupling this proton with the transferred neutron in the  $2d_{5/2}$  state. The  $0^-$  and  $1^-$  states of  ${}^{90}\text{Y}$  are obtained by coupling of the  $2p_{1/2}$  proton

TABLE III. Details of the  ${}^{90}\text{Y}$  transfer states included in the CRC calculations.

Energy (MeV)	$J^\pi$	$L$	Particle configuration	$C^2S$ [29]
0.000	$2^-$	1	$\pi 2p_{1/2} \nu 2d_{5/2}$	0.40
0.202	$3^-$	1	$\pi 2p_{1/2} \nu 2d_{5/2}$	0.63
0.682	$7^+$	4	$\pi 1g_{9/2} \nu 2d_{5/2}$	0.16
0.777	$2^+$	4	$\pi 1g_{9/2} \nu 2d_{5/2}$	0.10
0.953	$3^+$	4	$\pi 1g_{9/2} \nu 2d_{5/2}$	0.10
1.047	$5^+$	4	$\pi 1g_{9/2} \nu 2d_{5/2}$	0.12
1.189	$4^+$	4	$\pi 1g_{9/2} \nu 2d_{5/2}$	1.00
1.212	$0^-$	1	$\pi 2p_{1/2} \nu 3s_{1/2}$	1.00
1.298	$6^+$	4	$\pi 1g_{9/2} \nu 2d_{5/2}$	0.12
1.371	$1^-$	1	$\pi 2p_{1/2} \nu 3s_{1/2}$	1.00
1.417	$3^-$	1	$\pi 2p_{3/2} \nu 2d_{5/2}$	1.00
1.566	$4^-$	1	$\pi 2p_{3/2} \nu 2d_{5/2}$	1.20
1.647	$4^-$	3	$\pi 1f_{5/2} \nu 2d_{5/2}$	1.94
1.761	$2^-$	3	$\pi 1f_{5/2} \nu 2d_{5/2}$	0.83
2.030	$5^-$	3	$\pi 1f_{5/2} \nu 2d_{5/2}$	1.28

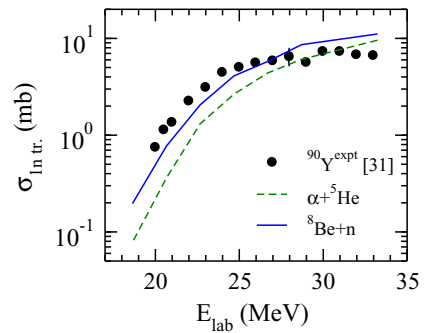


FIG. 7. (Color online) Comparison of the experimental  $1n$  transfer cross sections (filled circles) with the corresponding values obtained from the CDCC + CRC calculations. Errors on the experimental data are within the point size.

of  ${}^{89}\text{Y}$  with the transferred neutron going into the  $3s_{1/2}$  state. Higher excited states with energies between 1.4 MeV and 2 MeV form a multiplet due to coupling of the  $2p_{1/2}$  proton of  ${}^{89}\text{Y}$  with  $2d_{5/2}$ . States beyond 2 MeV were not included in the calculations due to mixture in the  $L$  values and thus uncertainties in the particle configurations. Even for the states up to 2 MeV the spectroscopic factors for only a few states were available. For all other states their value was taken to be 1.0 (see Table III). The binding potential for the transferred neutron was taken to be of the Woods-Saxon form with  $r_o = 1.25$  fm and  $a_o = 0.65$  fm. The depth of the potential was varied to reproduce the binding energy of the transfer state. In addition, a spin-orbit potential with  $V_{so} = 6.0$  MeV,  $r_{so} = 1.25$  fm, and  $a_{so} = 0.65$  fm was taken.

The  $1n$  transfer states were coupled along with the continuum + resonant states (CDCC + CRC), described in Secs. III B 1 and III B 2, and the results are plotted in Fig. 5 as dot-dashed lines. It is observed that coupling the  $1n$  transfer channel has no significant effect on the elastic scattering angular distribution and the results overlap with the CDCC results for both  $\alpha + {}^5\text{He}$  and  ${}^8\text{Be} + n$ . The  $1n$  transfer cross sections obtained from these calculations were compared with the experimental values obtained in Ref. [31] as shown in Fig. 7. The  ${}^8\text{Be} + n$  cluster calculations give an overall better agreement (solid line). The DPPs generated from the CDCC + CRC calculations using the two cluster structures have been plotted in Figs. 6(c), 6(d) and 6(g), 6(h), respectively.

### IV. INCLUSIVE BREAKUP- $\alpha$ CROSS SECTIONS

Due to the low breakup threshold energy for  ${}^9\text{Be}$ , a significant contribution to the reaction cross section is expected to be observed from the breakup- $\alpha$  cross section. It was observed that a broad peak in the  $\alpha$  spectrum is centered at an energy around  $(4/9)E({}^9\text{Be})$  [as seen in Fig. 1(b)], indicating that most of the  $\alpha$ 's are due to projectile breakup. Thus, from the present data, an attempt has been made to estimate the inclusive breakup- $\alpha$  cross sections, calculated from the  $\alpha$  band containing a contribution from the breakup/transfer processes, and it has been compared with the reaction cross section for each energy. In the  $\alpha$  band obtained in the spectra, there can be mixing of  $\alpha$  particles coming from fusion evaporation

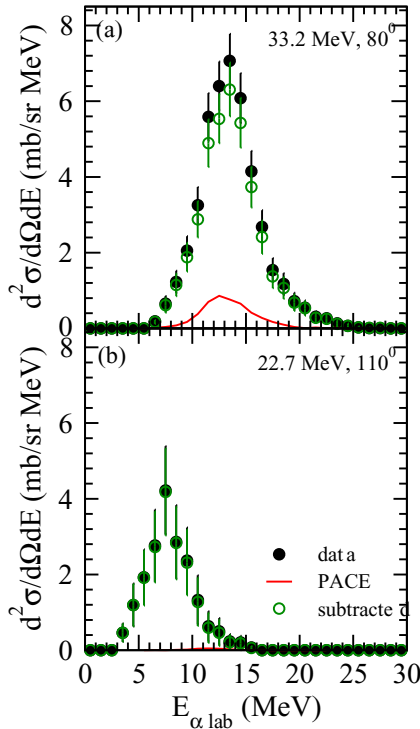


FIG. 8. (Color online) Double-differential inclusive breakup- $\alpha$  cross sections at (a) 33.2 MeV and  $80^\circ$  and (b) 22.7 MeV at  $110^\circ$ . The solid line represents the corresponding cross sections obtained from the statistical model code PACE and the unfilled circles the  $\alpha$  cross sections after subtraction from the PACE values.

residues. To check this, the experimental double-differential inclusive breakup- $\alpha$  cross sections have been compared with the corresponding values obtained from the statistical model code PACE [32] and has been plotted at two energies in Fig. 8, one above and one below the Coulomb barrier. It can be seen that the contribution of  $\alpha$  particles coming from the evaporation residues to the experimental  $\alpha$  band is negligible. We note here that at two lower energies, 24.7 and 22.7 MeV, extraction of inclusive  $\alpha$  cross sections has large error due to difficulty in separating the low-energy  $\alpha$  background coming from target contamination. It was not possible to estimate these errors from the data. Thus the error bars for these values have been increased by  $\sim 30\%$  to incorporate the above-mentioned uncertainties. The differential inclusive breakup- $\alpha$  cross sections have been calculated by taking the integral area of the peak in the spectra [Fig. 1(b)] and are plotted in Fig. 9 at different energies. These have been further integrated to obtain the total inclusive breakup- $\alpha$  cross section at each energy, plotted in Fig. 10(a) as unfilled triangles. These have been compared to the reaction cross sections obtained from OMA1 (solid line) and CDCC + CRC calculations done using  $\alpha + {}^5\text{He}$  (dashed) and  ${}^8\text{Be} + n$  clusters (dot-dashed line).

It is observed that the breakup- $\alpha$  cross sections form a large fraction of the reaction cross sections and are almost equal to them at below-barrier energies, a result similar to that observed for the  ${}^6\text{Li} + {}^{209}\text{Bi}$  system [33]. Thus it can be qualitatively said that the breakup channel is indeed the reaction channel

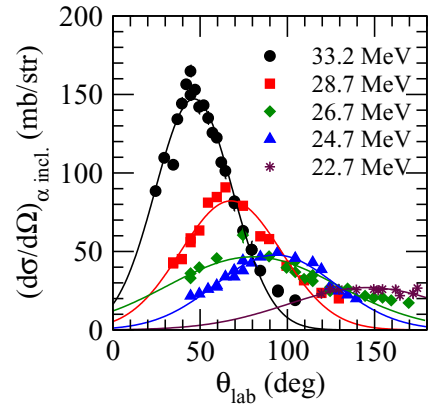


FIG. 9. (Color online) Differential inclusive breakup- $\alpha$  cross sections at different projectile beam energies.

present at below-barrier energies, which further supports the observation of the persistence of the imaginary potential in Figs. 3 and 4 at these energies, and thus the indication of the BTA behavior of the system. We also note here that the reaction cross sections obtained from OMA1 as well as CDCC + CRC calculations have reasonable overlap at

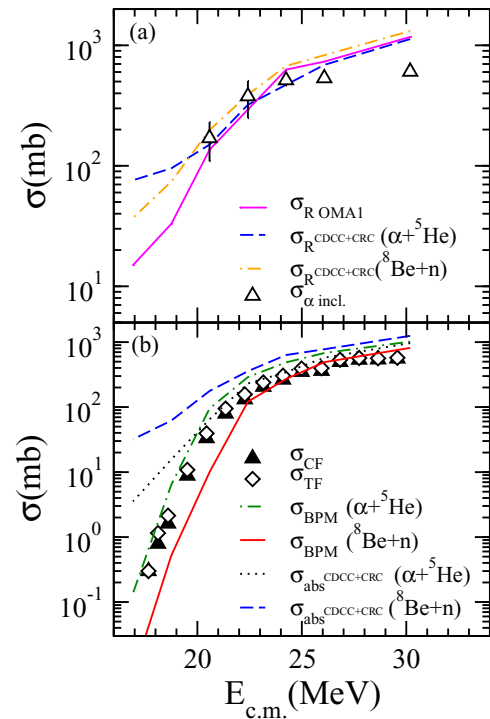


FIG. 10. (Color online) (a) Comparison between the reaction cross sections obtained from OMA1 (solid line) and from CDCC + CRC calculations using  $\alpha + {}^5\text{He}$  (dashed line) and  ${}^8\text{Be} + n$  (dot-dashed line), and the inclusive breakup- $\alpha$  cross sections (unfilled triangles) as a function of energy. (b) Comparison of the experimental CF and TF cross sections with the absorption cross sections obtained from the long-ranged imaginary potential using  $\alpha + {}^5\text{He}$  (dotted line) and  ${}^8\text{Be} + n$  (dashed line) obtained in the CDCC + CRC calculations and the BPM fusion obtained using  $\alpha + {}^5\text{He}$  (dot-dashed line) and  ${}^8\text{Be} + n$  (solid line).

above-barrier energies which is also reflected in similar fits to the elastic scattering angular distributions at these energies. However, for below-barrier energies they differ significantly. This might be due to the explicit couplings included in the CDCC + CRC calculations which might lead to enhanced cross sections at lower energies as compared to the OMA1 results, which artificially take into account absorption from the elastic channel via an imaginary potential.

## V. FUSION AND REACTION CROSS SECTIONS

A simultaneous description of the elastic and fusion data was attempted by comparing the experimental CF cross sections [31] for the system (filled triangles) with the absorption cross section due to the long-ranged imaginary potentials (dashed line) obtained from the CDCC + CRC calculations (dotted and dashed lines), which satisfactorily reproduce the experimental elastic angular distributions, and the barrier penetration model (BPM) [34] calculations (dot-dashed and solid lines) using both  $\alpha + {}^5\text{He}$  and  ${}^8\text{Be} + n$  [Fig. 10(b)]. The CF cross sections have been observed to be suppressed at above-barrier energies with respect to the BPM values obtained from the  ${}^8\text{Be} + n$  cluster calculations, by about  $\sim 20\% - 25\%$ , which is consistent within errors with the observed suppression in [31]. Similar results have been observed for the  ${}^6\text{Li} + {}^{209}\text{Bi}$  system [35]. However, the CF cross sections show more than 25% suppression with respect to BPM results obtained from  $\alpha + {}^5\text{He}$  cluster calculations. As compared to the absorption cross sections, the CF cross sections have been observed to be suppressed over the entire energy range. Further, a lower limit of the experimental total fusion [TF = CF + incomplete fusion (ICF)] cross sections (unfilled diamonds) has also been compared with the absorption cross sections, and the former have been observed to be overestimated in the entire energy range. There can be two reasons for this: (i) Only a lower limit of the TF cross sections could be obtained for the system, due to the lower limit of the ICF cross sections measured experimentally. This is because one of the evaporation residues corresponding to the ICF channel ( ${}^{92}\text{Nb}^g$ ) had a large half-life ( $\sim 3.47 \times 10^7$  yr) and thus could not be measured via the offline  $\gamma$ -counting method [31]. (ii) The absorption cross sections are obtained from long-ranged imaginary potentials to reproduce the elastic scattering data and thus might contain an additional contribution due to absorption of flux from channels not included in the calculations.

Finally, the average values of the reaction cross sections obtained from the OMA1 and OMA2 for the  ${}^9\text{Be} + {}^{89}\text{Y}$  system have been compared in Fig. 11(a) to the corresponding values obtained for nearby systems involving tightly bound and weakly bound stable as well as unstable nuclei as was done in Ref. [43]. The cross sections have been reduced according to  $\sigma_{\text{red}} = \sigma_R / (A_p^{1/3} + A_t^{1/3})^2$  while the energies have been reduced according to  $E_{\text{red}} = E_{\text{c.m.}}(A_p^{1/3} + A_t^{1/3}) / (Z_p Z_t)$  in order to eliminate the geometrical effect on the cross sections for the different systems. For the sake of completeness, in Fig. 11(b), the reduced reaction cross section for the  ${}^9\text{Be} + {}^{89}\text{Y}$  system have also been compared with the corresponding values involving  ${}^9\text{Be}$  and different target nuclei studied. It can be seen that the cross sections for the systems involving weakly

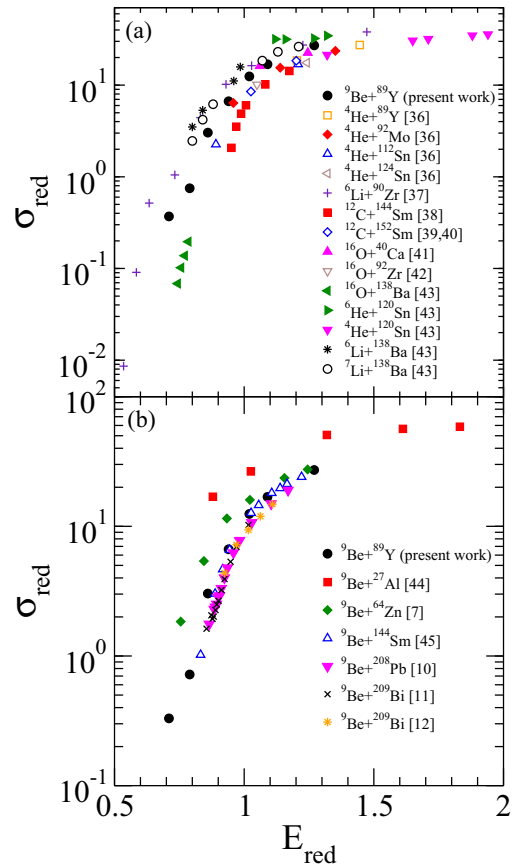


FIG. 11. (Color online) Comparison of reduced reaction cross sections for different systems.

bound stable as well as unstable nuclei are higher compared to those involving the tightly bound nuclei. The observed enhancement in the reaction cross sections indicates that in addition to possible nonelastic channels as in the tightly bound nuclei, the extra contribution to the reaction cross sections must come from the weakly bound nature of the nuclei due to the breakup channel being one of the dominant reaction channels. In Fig. 11(b), the reaction cross sections for the  ${}^9\text{Be} + {}^{89}\text{Y}$  system are found to be consistent with the corresponding values obtained from  ${}^9\text{Be}$  scattering from the heavier targets.

## VI. SUMMARY AND CONCLUSIONS

To summarize, elastic scattering measurement has been carried out for the  ${}^9\text{Be} + {}^{89}\text{Y}$  system at near-barrier energies with the aim of investigating the effect of the breakup channel on the elastic channel. Optical model analysis has been carried out and the energy dependence of the real and imaginary parts of the optical potential investigated by applying a dispersion relation, from which an indication of BTA behavior for the system is seen. To further investigate this, CDCC calculations have been carried out using both the  $\alpha + {}^5\text{He}$  and  ${}^8\text{Be} + n$  cluster structures for  ${}^9\text{Be}$ . An overall better agreement of the experimental angular distributions with the calculations has been observed for calculations done using  ${}^8\text{Be} + n$  especially at below-barrier energies, suggesting the importance of this

cluster structure at these energies. This is in agreement with the observations in Ref. [20]. An overall repulsive nature of the DPP is observed from the CDCC calculations using the  $\alpha + {}^5\text{He}$  cluster while from those done using  ${}^8\text{Be} + n$ , the DPP is observed to be attractive, especially at below-barrier energies.

$1n$  transfer calculations have been carried out within the CRC framework by coupling them along with the continuum states. Inclusion of this channel does not have a significant effect on the elastic scattering angular distributions. A reasonable agreement between the experimental  $1n$  transfer cross sections with the calculated values using the  ${}^8\text{Be} + n$  cluster structure for  ${}^9\text{Be}$  is observed.

Inclusive breakup- $\alpha$  cross sections have been extracted from the data and compared with the reaction cross sections obtained from the OMA as well as from the CDCC + CRC calculations, in order to understand which are the dominant channels contributing to the reaction channels at below-barrier energies. The former are observed to form a large fraction of the reaction cross sections and are almost equal to the latter at below-barrier energies. This is indicative of the presence of the breakup channel even at lower energies, which is also reflected in the energy dependence of the OMA for the system, where the imaginary part is observed to persist even at below-barrier energies.

A simultaneous description of the elastic and fusion cross sections has been attempted for the system. For this, a comparison of the absorption cross sections obtained from the long-ranged imaginary potential used in the CDCC + CRC calculations, which reasonably reproduce the experimental elastic scattering angular distributions, and the BPM fusion has been made with the experimental CF and TF [31] cross sections. Both the CF and TF cross sections have been observed to be suppressed compared to the absorption cross sections in

the entire energy range. As compared to the cross sections obtained from the BPM calculations, the CF cross sections have been found to be suppressed between 20% and 25%, which is consistent within errors to the suppression observed in [31]. The observed suppression of the TF cross sections, however, may have the following causes: (i) Only a lower limit of ICF cross sections was obtained in the fusion measurement, and thus only a lower limit of TF cross sections could be compared; (ii) the long-ranged imaginary potential used in the CRC calculations, in order to reproduce the elastic scattering data, may lead to excess of absorption cross sections due to absorption of flux from channels not included in the calculations.

The reaction cross sections for the  ${}^9\text{Be} + {}^{89}\text{Y}$  system have been compared with the corresponding values for nearby systems consisting of tightly bound as well as weakly bound stable and unstable nuclei. The cross sections for the  ${}^9\text{Be} + {}^{89}\text{Y}$  system are enhanced as compared to the tightly bound systems, consistent with the observations in Ref. [43]. This indicates that the enhanced cross sections must be due to the weakly bound nature of  ${}^9\text{Be}$ , since in addition to the nonelastic channels, as in the tightly bound nuclei, the breakup channel is also one of the dominant channels in reactions involving weakly bound nuclei at near-barrier energies.

#### ACKNOWLEDGMENTS

The authors would like to thank the Pelletron Accelerator staff for smooth operation of the machine during the experiment, Dr. Y. K. Gupta from NPD, BARC for providing the target, and Mr. P. Patale for his help during the experiment. One of the authors (V.V.P.) acknowledges financial support through the INSPIRE faculty program, from the Department of Science and Technology, Government of India, in carrying out these investigations.

- 
- [1] L. F. Canto, P. R. S. Gomes, R. Donangelo, and M. S. Hussein, *Phys. Rep.* **424**, 1 (2006), and references therein.
- [2] N. Keeley, R. Raabe, N. Alamanos, and J. L. Sida, *Prog. Part. Nucl. Phys.* **59**, 579 (2007), and references therein.
- [3] G. R. Satchler, *Phys. Rep.* **199**, 147 (1991).
- [4] C. Mahaux, H. Ngo, and G. R. Satchler, *Nucl. Phys. A* **449**, 354 (1986).
- [5] R. A. N. Oliveira, N. Carlin, R. Liguori Neto, M. M. de Moura, M. G. Munhoz, M. G. del Santo, F. A. Souza, E. M. Szanto, A. Szanto de Toledo, and A. A. P. Suaide, *Nucl. Phys. A* **856**, 46 (2011).
- [6] S. B. Moraes, P. R. S. Gomes, J. Lubian, J. J. S. Alves, R. M. Anjos, M. M. Sant'Anna, I. Padron, C. Muri, R. Liguori Neto, and N. Added, *Phys. Rev. C* **61**, 064608 (2000).
- [7] P. R. S. Gomes, M. D. Rodríguez, G. V. Martí, I. Padron, L. C. Chamon, J. O. Fernández Niello, O. A. Capurro, A. J. Pacheco, J. E. Testoni, A. Arazi, M. Ramírez, R. M. Anjos, J. Lubian, R. Veiga, R. Liguori Neto, E. Crema, N. Added, C. Tenreiro, and M. S. Hussein, *Phys. Rev. C* **71**, 034608 (2005).
- [8] A. Gomez Camacho, P. R. S. Gomes, J. Lubian, and L. F. Canto, *Phys. Rev. C* **82**, 014616 (2010).
- [9] A. Gomez Camacho, P. R. S. Gomes, J. Lubian, and I. Padron, *Phys. Rev. C* **77**, 054606 (2008).
- [10] R. J. Woolliscroft, B. R. Fulton, R. L. Cowin, M. Dasgupta, D. J. Hinde, C. R. Morton, and A. C. Berriman, *Phys. Rev. C* **69**, 044612 (2004).
- [11] N. Yu, H. Q. Zhang, H. M. Jia, S. T. Zhang, M. Ruan, F. Yang, Z. D. Wu, X. X. Xu, and C. L. Bai, *J. Phys. G* **37**, 075108 (2010).
- [12] C. Signorini, A. Andrighetto, M. Ruan, J. Y. Guo, L. Stroe, F. Soramel, K. E. G. Lobner, L. Muller, D. Pierroutsakou, M. Romoli, K. Rudolph, I. J. Thompson, M. Trotta, A. Vitturi, R. Gernhauser, and A. Kastennmuller, *Phys. Rev. C* **61**, 061603(R) (2000).
- [13] I. J. Thompson, *Comput. Phys. Rep.* **7**, 167 (1988).
- [14] <http://www.srim.org>.
- [15] G. R. Satchler and W. G. Love, *Phys. Rep.* **55**, 183 (1979).
- [16] V. Hnizdo, J. Szymakowski, K. W. Kemper, and J. D. Fox, *Phys. Rev. C* **24**, 1495 (1981).
- [17] H. De Vries, C. W. De Jager, and C. De Vries, *At. Data Nucl. Data Tables* **36**, 495 (1987).

- [18] J. Cook, *Comput. Phys. Commun.* **25**, 125 (1982).
- [19] S. K. Pandit, V. Jha, K. Mahata, S. Santra, C. S. Palshetkar, K. Ramachandran, V. V. Parkar, A. Shrivastava, H. Kumawat, B. J. Roy, A. Chatterjee, and S. Kailas, *Phys. Rev. C* **84**, 031601(R) (2011).
- [20] V. V. Parkar, V. Jha, S. K. Pandit, S. Santra, and S. Kailas, *Phys. Rev. C* **87**, 034602 (2013).
- [21] N. Keeley, K. W. Kemper, and K. Rusek, *Phys. Rev. C* **64**, 031602 (2001).
- [22] H. J. Votava, T. B. Clegg, E. J. Ludwig, and W. J. Thompson, *Nucl. Phys. A* **204**, 529 (1973).
- [23] G. G. Kiss, P. Mohr, Zs. Fülöp, D. Galaviz, Gy. Gyürky, Z. Elekes, E. Somorjai, A. Kretschmer, K. Sonnabend, A. Zilges, and M. Avrigeanu, *Phys. Rev. C* **80**, 045807 (2009).
- [24] M. Nolte, H. Machner, and J. Bojowald, *Phys. Rev. C* **36**, 1312 (1987).
- [25] S. Dixit, W. Bertozzi, T. N. Buti, J. M. Finn, F. W. Hersman, C. E. Hyde-Wright, M. V. Hynes, M. A. Kovash, B. E. Norum, J. J. Kelly, A. D. Bacher, G. T. Emery, C. C. Foster, W. P. Jones, D. W. Miller, B. L. Berman, and D. J. Millener, *Phys. Rev. C* **43**, 1758 (1991).
- [26] D. R. Tilley, J. H. Kelley, J. L. Godwin, D. J. Millener, J. E. Purcell, C. G. Sheu, and H. R. Weller, *Nucl. Phys. A* **745**, 155 (2004).
- [27] J. Lang, R. Müller, J. Unternährer, L. Jarczyk, B. Kamys, and A. Strzalkowski, *Phys. Rev. C* **16**, 1448 (1977).
- [28] A. J. Koning, and J. P. Delaroche, *Nucl. Phys. A* **713**, 231 (2003).
- [29] E. Browne, *Nucl. Data Sheets* **82**, 379 (1997).
- [30] S. Michaelsen, A. Harder, K. P. Lieb, G. Graw, R. Hertenberger, D. Hofer, P. Schiemenz, E. Zanotti, H. Lenske, A. Weigel, H. H. Wolter, S. J. Robinson, and A. P. Williams, *Nucl. Phys. A* **552**, 232 (1993), and references therein.
- [31] C. S. Palshetkar, S. Santra, A. Chatterjee, K. Ramachandran, Shital Thakur, S. K. Pandit, K. Mahata, A. Shrivastava, V. V. Parkar, and V. Nanal, *Phys. Rev. C* **82**, 044608 (2010).
- [32] A. Gavron, *Phys. Rev. C* **21**, 230 (1980).
- [33] S. Santra, S. Kailas, V. V. Parkar, K. Ramachandran, V. Jha, A. Chatterjee, P. K. Rath, and A. Parihari, *Phys. Rev. C* **85**, 014612 (2012).
- [34] K. Rusek, N. Alamanos, N. Keeley, V. Lapoux, and A. Pakou, *Phys. Rev. C* **70**, 014603 (2004).
- [35] S. Santra, S. Kailas, K. Ramachandran, V. V. Parkar, V. Jha, B. J. Roy, and P. Shukla, *Phys. Rev. C* **83**, 034616 (2011).
- [36] P. Mohr, D. Galaviz, Zs. Fülöp, Gy. Gyürky, G.G. Kiss, and E. Somorjai, *Phys. Rev. C* **82**, 047601 (2010).
- [37] H. Kumawat, V. Jha, B.J. Roy, V.V. Parkar, S. Santra, V. Kumar, D. Dutta, P. Shukla, L.M. Pant, A.K. Mohanty, R.K. Choudhury, and S. Kailas, *Phys. Rev. C* **78**, 044617 (2008).
- [38] D. Abriola, A.A. Sonzogni, M. di Tada, A. Etchegoyen, M.C. Etchegoyen, J.O. Fernández Niello, S. Gil, A.O. Macchiavelli, A.J. Pacheco, R. Piegai, and J.E. Testoni, *Phys. Rev. C* **46**, 244 (1992).
- [39] R. Broda, M. Ishihara, B. Herskind, H. Oeschler, S. Ogaza, and H. Hyde, *Nucl. Phys. A* **248**, 356 (1975).
- [40] Kui Zhao, Xiuqin Lu, Yehao Cheng, Qingli Li, Min Li, Zhichang Li, Jiyou Guo, Shuyuan Li, Qinghua Zhang, Xiaobin Song, and Chenglie Jiang, *Z. Phys. A* **348**, 95 (1994).
- [41] J. Orloff and W. W. Daehnick, *Phys. Rev. C* **3**, 430 (1971).
- [42] E.M. Takagui, G.R. Satchler, H. Takai, K. Koide, and O. Dietzsch, *Nucl. Phys. A* **514**, 120 (1990).
- [43] P. N. de Faria, R. Lichtenthäler, K. C. C. Pires, A. M. Moro, A. Lépine-Szily, V. Guimarães, D. R. Mendes, Jr., A. Arazí, M. Rodríguez-Gallardo, A. Barioni, V. Morcelle, M. C. Morais, O. Camargo, Jr., J. Alcantara Nuñez, and M. Assunção, *Phys. Rev. C* **81**, 044605 (2010).
- [44] G. V. Martí, P.R.S. Gomes, M.D. Rodríguez, J.O. Fernández Niello, O.A. Capurro, A.J. Pacheco, J.E. Testoni, M. Ramirez, A. Arazí, I. Padron, R.M. Anjos, J. Lubian, and E. Crema, *Phys. Rev. C* **71**, 027602 (2005).
- [45] P. R. S. Gomes, I. Padron, E. Crema, O. A. Capurro, J. O. Fernández Niello, A. Arazí, G. V. Martí, J. Lubian, M. Trotta, A. J. Pacheco, J. E. Testoni, M. D. Rodríguez, M. E. Ortega, L. C. Chamon, R. M. Anjos, R. Veiga, M. Dasgupta, D. J. Hinde, and K. Hagino, *Phys. Rev. C* **73**, 064606 (2006).